

Stellar feedback drives the baryon deficiency in low-mass galaxies

Haoran Yu^{1,2}, Enci Wang^{1,2*}, Zeyu Chen^{1,2}, Céline Péroux^{3,4},
Hu Zou⁵, Zhicheng He^{1,2}, Huiyuan Wang^{1,2}, Cheqiu Lyu^{1,2},
Cheng Jia^{1,2}, Chengyu Ma^{1,2}, Xu Kong^{1,2}

¹Department of Astronomy, University of Science and Technology of China,
Hefei 230026, People's Republic of China

²School of Astronomy and Space Science, University of Science and Technology of China,
Hefei 230026, People's Republic of China

³European Southern Observatory, Karl-Schwarzschild-Str. 2,
85748 Garching-bei-München, Germany

⁴Aix Marseille Université, CNRS, LAM (Laboratoire d'Astrophysique de Marseille)
UMR 7326, 13388, Marseille, France

⁵National Astronomical Observatories, Chinese Academy of Sciences,
Beijing 100012, People's Republic of China

*Corresponding author. Email: ecwang16@ustc.edu.cn

Stellar feedback, as a key process regulating the baryon cycle, is thought to greatly redistribute baryonic material inside and outside the dark matter halos (DMHs), however the observational evidences are lacking. Through stacking

analyses of $\sim 400,000$ galaxy spectra from Dark Energy Spectroscopic Instrument (DESI), we find star formation driven cool outflows in Mg II absorption line. Assuming only gravity acts on the launched gas, our calculations reveal that outflows from low mass galaxies ($M_* < 10^{10} M_\odot$) are capable of escaping beyond the DMHs, which aligns well with our finding in the circumgalactic medium (CGM) absorption along the minor-axes of galaxies using background quasars. This research offers indirect evidence that stellar feedback drives the low baryon retention rate in low-mass haloes, implicating that baryonic processes within galaxies are connected with the diffuse matter beyond the DMHs.

Introduction

Star-forming galaxies undergo intense baryon processes within their interiors, interacting with the surrounding environments during their lifetimes. These processes include gas accretion from the surrounding environments (1), gas cooling and collapse due to gravitational instability (2), gas consumption during star formation, and stellar feedback in the form of stellar winds and supernova explosions, driving outflows in galactic scale (3–5). In numerical simulations of galaxy formation and evolution, gas ejection launched by stellar feedback is introduced to explain the low baryon retention fraction in galaxies (6–9). However, hindered by the limited information about the multi-phase baryon processes from observations, no clear evidence has justified the connection between the baryon deficiency in galaxies and the feedback processes. In the meantime, the physical mechanisms of feedback processes, which are interpreted quite differently in various suits of simulations (10–14). The critical observational evidence is of urgent need, potentially challenging the theory of galaxy evolution.

In this work, we meticulously study the cool outflows in star-forming galaxies through utilizing tremendous amount of galaxy spectra from the early data release of Dark Energy Spectroscopic Instrument (15) (DESI EDR). Through spectral stacking analysis, we derive statistically robust composite galaxy spectra for galaxies of different stellar masses (M_*) and star-formation rates (SFR). We find cool outflows prevalent in star-forming galaxies in the form of blueshifted absorption line of singly ionized magnesium (Mg II). Through combined analysis of Mg II absorption in the CGM

surrounding those galaxies using background QSOs, we for the first time provide observational evidence that stellar feedback drives strong enough outflows to cause the baryon deficiency in low-mass galaxies.

Results

Analogous to the Hertzsprung–Russell diagram in stellar evolution, the Star-Forming Main Sequence (SFMS) (16–18) — a fundamental correlation between M_* and SFR — serves as a critical framework for investigating galaxy evolution. We stack galaxy spectra based on their positions within the SFMS, as shown in the left panel of Figure 1. The samples are binned into hexagonal regions with a width length of 0.05 dex, while the peripheral ones enclosing fewer than 500 galaxies are excluded. The color of each hexagon corresponds to the amount of spectra within that bin and its adjacent neighbors, which are combined to obtain the stacked spectra. With most bins containing more than 10,000 spectra, the resulting stacked spectra achieve exceptionally high signal-to-noise ratio ($S/N \gtrsim 100$), as demonstrated in the inset.

Using the BOXCAR method (19), we extract the outflow equivalent width (EW_{out}) and v_{out} of the Mg II absorption features from the composite spectra, as shown in the top-right panels of Figure 1. Assuming the geometry of the outflow to be an expanding spherical thin shell launching at 5 kpc (see Methods (20)) and adopting an empirical relation between the equivalent width of Mg II absorption and the column density of neutral hydrogen (21), we derive mass outflow rate \dot{M}_{out} and mass loading factor $\eta \equiv \dot{M}_{\text{out}}/\text{SFR}$, as shown in the bottom-right panels of Figure 1.

As shown, EW_{out} increases significantly with increasing SFR, while shows relatively weak dependence on M_* . We observe that the mean velocity of the outflowing gas is more correlated with M_* , whereas no significant dependence on SFR emerges at given stellar mass. Similar dependency of v_{out} on M_* for low-mass galaxies has also been found in the energy-driven wind in simulations (22), suggesting that the cool-phase gas traced by Mg II is basically in an energy-conserving regime. On the other hand, \dot{M}_{out} and η have strong dependence on SFR, confirming the stellar feedback-driven outflow scenario (23). Our findings offer valuable observational insights into the effects of stellar feedback, providing constraints on the small-scale feedback mechanisms implemented in simulations.

The sample covers a broad redshift range, allowing us to investigate the above results across different redshift intervals. The results are shown in Figure 2. The correlation between v_{out} and M_* is nearly identical for the three redshift bins, which can be written as an empirical relation:

$$\frac{v_{\text{out}}}{\text{km s}^{-1}} = (85.3 \pm 2.7) \cdot \log \left(\frac{M_*}{10^{10} M_{\odot}} \right) + (269.8 \pm 0.9). \quad (1)$$

This shows that the v_{out} increases $\sim 85 \text{ km s}^{-1}$ when the stellar mass increases 1 dex, with the typical mean outflow velocity to be $\sim 270 \text{ km s}^{-1}$ for a galaxy with stellar mass of $10^{10} M_{\odot}$. The Mg II absorption-line-derived outflow velocities taken from literature (19, 24) are presented panel A for comparison. The relation between v_{out} and SFR is less tight across different redshift bins, indicating that it could be the byproduct of the correlation between v_{out} and M_* . Similarly, we find the relation between \dot{M}_{out} and SFR almost independent of redshift, which is

$$\frac{\dot{M}_{\text{out}}}{M_{\odot} \text{ yr}^{-1}} = (34.5 \pm 0.6) \cdot \log \left(\frac{\text{SFR}}{10 M_{\odot} \text{ yr}^{-1}} \right) + (31.1 \pm 0.3). \quad (2)$$

The \dot{M}_{out} as a function of M_* for different redshifts shows significant deviations, each exhibiting a nearly constant value. This again confirms that the outflow mass reflect the level of overall star formation, and the evolution of the outflow properties is primarily driven by the evolution of SFR along the cosmic time.

Discussion

The driving mechanisms of stellar feedback launched outflows have been extensively debated through observations of multi-phase outflows (25–28). Current theoretical frameworks fundamentally bifurcate into two paradigms: (i) energy-driven flows where supernova (SNe) energy injection dominates radiative losses, and (ii) momentum-driven regimes where radiation pressure governs outflow dynamics (4). In energy-driven scenario, the injected energy scale with SFR (29), $\dot{E} \propto \text{SFR}$, predicting a mass-loading factor scaling $\eta \propto v_{\text{out}}^{-2}$. Conversely, momentum-driven models yield $\eta \propto v_{\text{out}}^{-1}$ (30). We therefore show the relation between η and v_{out} in Figure 3, excluding massive systems with $M_* > 10^{10} M_{\odot}$ where contamination from active galactic nuclei (AGNs) could suppress measurements of η (see Methods (20) for evaluation of the contamination). We note that for high-redshift ($1.2 \leq z \leq 1.7$) sample η is lower than other bins especially for massive galaxies, which we speculate to be relevant to the higher SFR at high- z . We fit the data to models with slope of -1 and

−2, and calculate the Bayesian evidence to compare the models. The nested sampling analysis (31) yields a decisive Bayes factor of $\log K = 5.38$, strongly supporting the energy-driven scenario. This provides crucial evidence that radiative losses remain secondary to mechanical energy injection in galaxies, resolving long-standing discrepancies in feedback prescriptions.

To determine whether the outflow can escape from the host galaxy, we calculate its velocity decay during propagation, adopting a Navarro-Frenk-White (NFW) DMH model (32) and an exponential stellar disk (33). Assuming the outflow is launched at 5 kpc from the stellar disk with the observed v_{out} , we examine how the velocity varies as its kinetic energy is converted into gravitational potential energy, as shown in the top panel of Figure 4. We find that although the launch velocity of outflows in massive galaxies is higher, the gas cannot travel further than 100 kpc before falling back into the galaxy. In contrast, outflows in galaxies with $M_* \lesssim 10^{10} M_\odot$ are more likely to escape from the gravity potential and enrich the surrounding environment. This phenomenon is confirmed by studies of CGM metal absorption along the minor-axes of galaxies using background quasars (34), as shown in the bottom panel of Figure 4. As the stellar mass exceeds $10^{10} M_\odot$, the EW(Mg II) in the CGM between 20–150 kpc is significantly suppressed at the minor-axes, where the CGM is thought to be enriched by the bi-conical galactic outflows (35). This is opposite to the trend at the major-axes, where the CGM may be dominated by the inflowing gas (36). Our analysis highlights that the cool outflows in low-mass galaxies can effectively escape from the gravity potential of the host DMHs. This provides critical evidence that stellar feedback causes the baryon deficiency at the low-mass end of the galaxy population, emphasizing that stellar feedback plays a role in understanding the missing baryon problem in the low redshift universe (37).

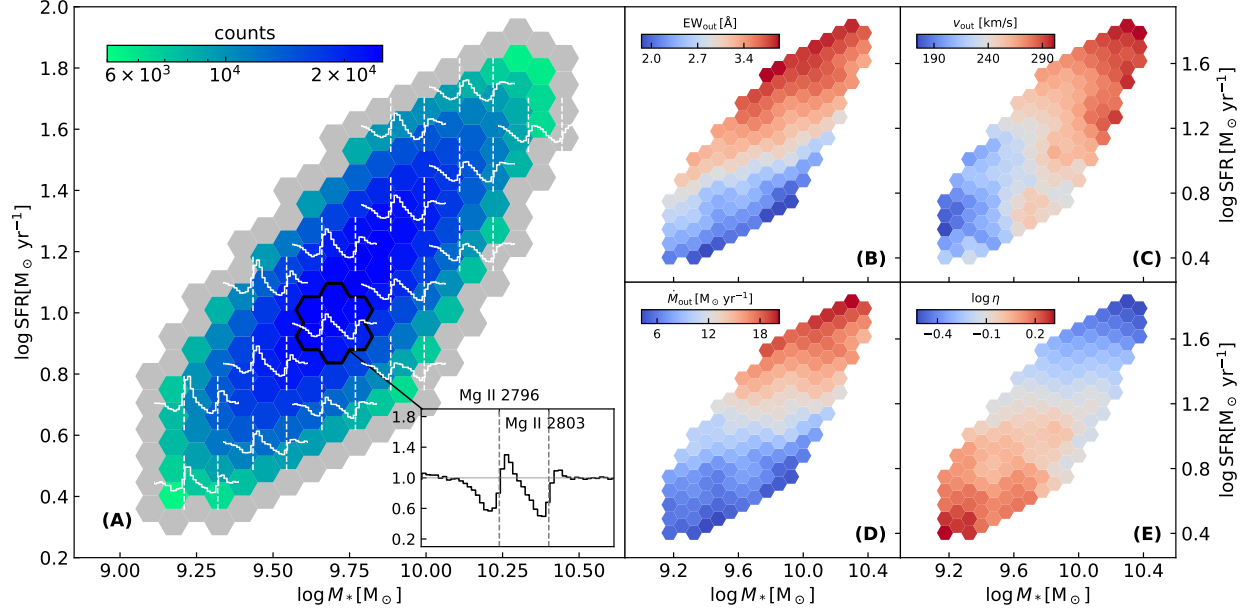


Figure 1: Outflow properties of samples with $0.6 < z < 1.7$ on the M_* -SFR diagram. (A) The distribution of samples, where colors of the hexagons indicate the total galaxy count per bin (including adjacent bins for stacking). Grey hexagons are excluded from color mapping due to insufficient neighboring bins, but the sample within them are used in the stacking of adjacent inner bins. Some of the stacked spectra are plotted over the hexagons with the two vertical dashed lines indicating the rest-frame wavelengths of Mg II $\lambda 2796$ and Mg II $\lambda 2803$, highlighting the prevalence of blueshifted outflow absorption features. The inset illustrates the stacked spectrum derived from galaxies within the black contour. **(B)** The map of outflow equivalent width (EW_{out}). **(C)** The map of mean outflow velocity (v_{out}). **(D)** The map of mass outflow rate (\dot{M}_{out}). **(E)** The map of mass-loading factor ($\eta \equiv \dot{M}_{\text{out}}/\text{SFR}$), where the values are derived from the stacked spectra.

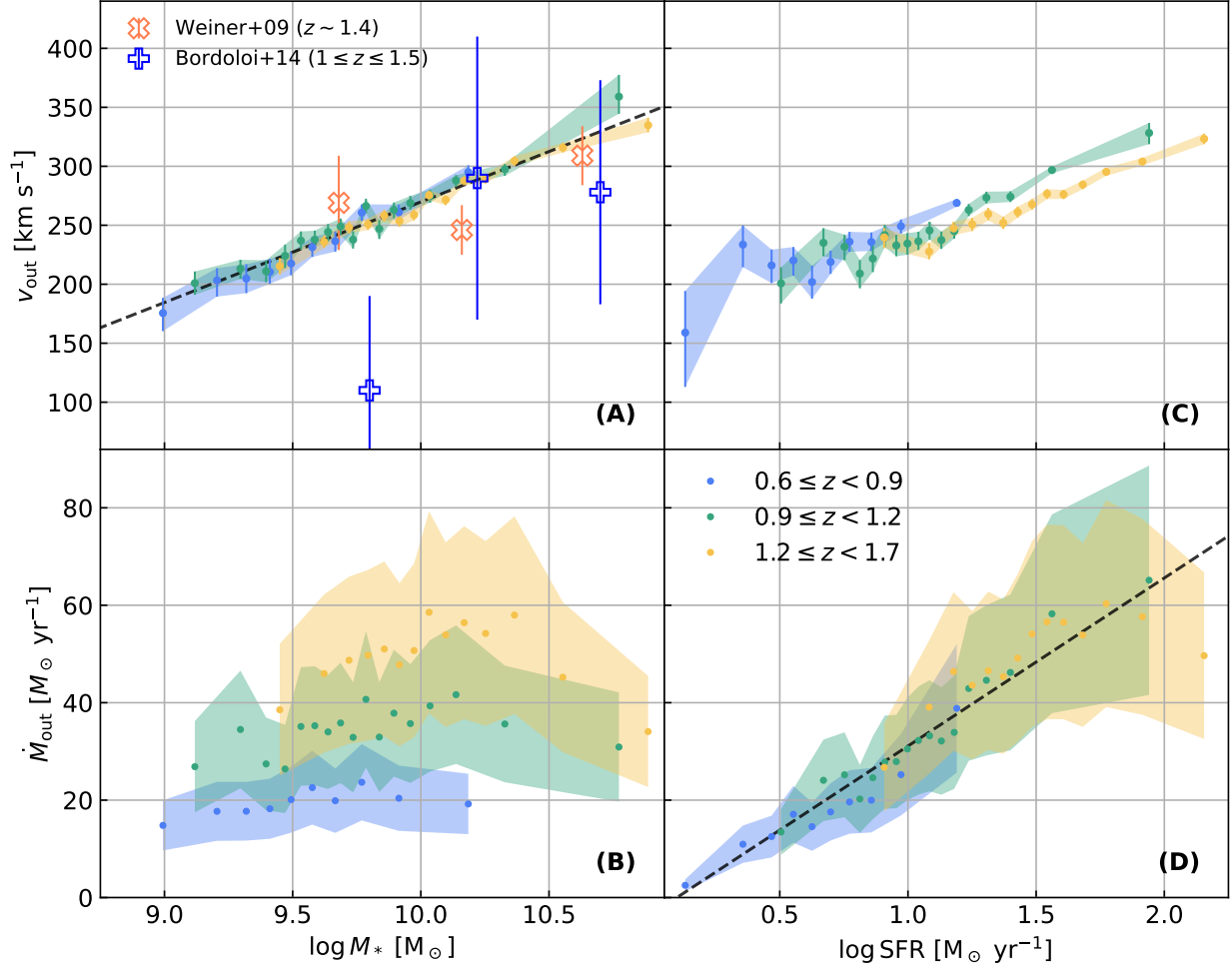


Figure 2: Redshift evolution of outflow properties. (A) v_{out} as a function of $\log M_*$. The samples are divided into three bins by redshift. The blue, green and yellow points represent the samples with $0.6 \leq z < 0.9$, $0.9 \leq z < 1.2$ and $1.2 \leq z < 1.7$, respectively. The open symbols denote Mg II outflow velocity measurements (19, 24) from the literature. The value of each point is derived with a composite spectrum of 10,000 spectra, with the shaded area indicating 1σ uncertainties from bootstrapping analysis. The dashed line is the best-fit relation, see Equation 1. (B) v_{out} as a function of $\log \text{SFR}$. (C) \dot{M}_{out} as a function of $\log M_*$. The shaded area indicates 1σ uncertainties propagated from the uncertainty in EW_{out} derived from bootstrap sampling and the uncertainty in estimating H I column density from EW_{out} . (D) \dot{M}_{out} as a function of $\log \text{SFR}$. The dashed line is the best-fit relation, see Equation 2.

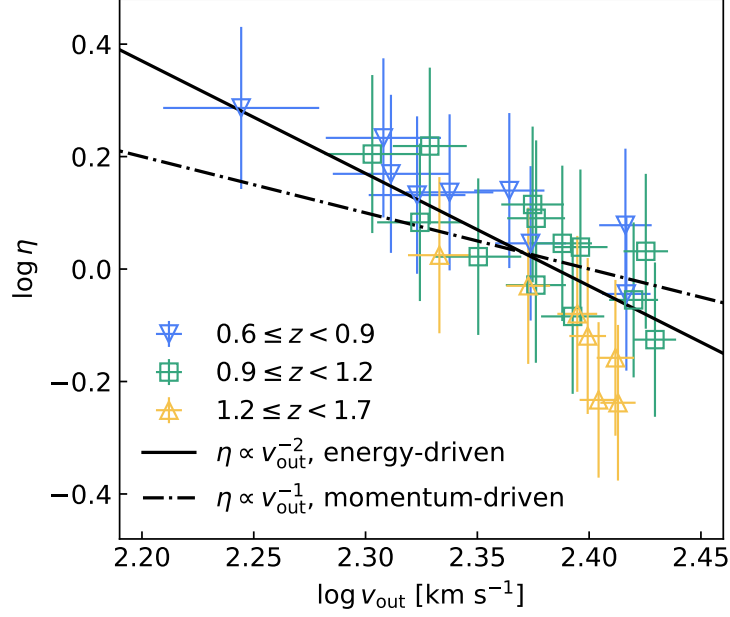


Figure 3: The mass-loading factor as a function of outflow velocity, distinguishing energy-driven and momentum-driven outflow regimes. The data points colored by redshift are taken from the left panel of Figure 2. To mitigate potential contamination from AGN activity in massive galaxies, we exclude data points with $M_* > 10^{10} M_\odot$. The solid and dash-dotted lines show best-fit models assuming fixed power-law exponents of -2 (energy-driven scenario) and -1 (momentum-driven scenario), respectively.

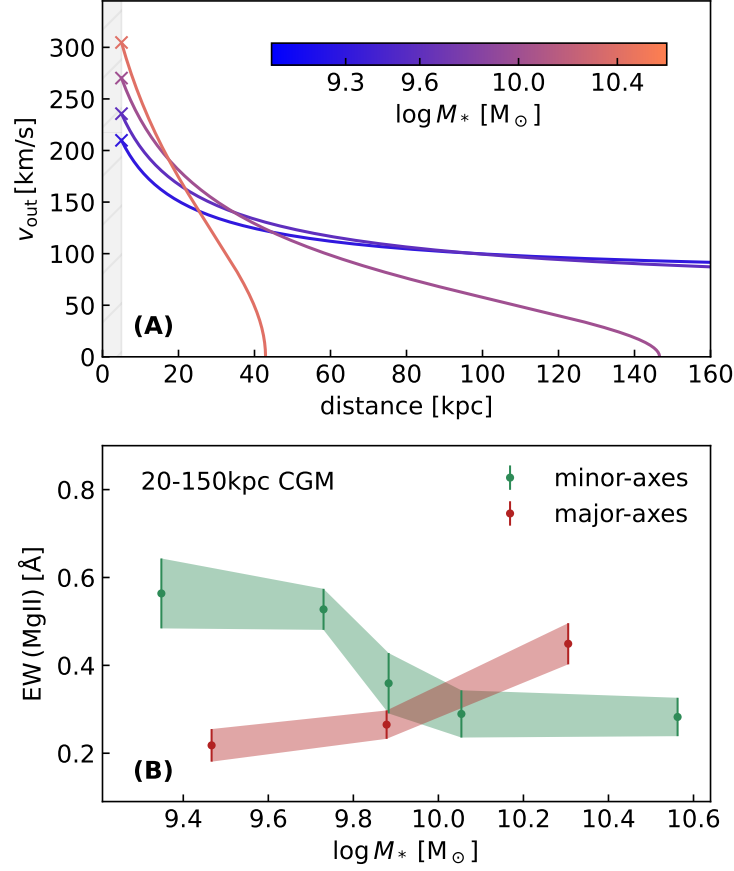


Figure 4: **(A)** The velocity decay of outflows. The diagonal crosses represent the observed outflow velocities, which are obtained through Equation 1 according to the given M_* of galaxies. The four curves with increasing launching velocity represent velocity decay of outflows in galaxies with stellar mass of $10^{9.3} M_\odot$, $10^{9.6} M_\odot$, $10^{10.0} M_\odot$ and $10^{10.4} M_\odot$. **(B)** The $\text{EW}(\text{Mg II})$ in the 20-150 kpc CGM surrounding galaxies derived using background quasars. The green (red) symbols represents CGM at the minor (major)-axes of the galaxy (see (20)).

References and Notes

1. F. van de Voort, J. Schaye, C. M. Booth, M. R. Haas, C. Dalla Vecchia, The rates and modes of gas accretion on to galaxies and their gaseous haloes. *Mon. Not. R. Astron. Soc.* **414** (3), 2458–2478 (2011), doi:10.1111/j.1365-2966.2011.18565.x.
2. T. A. Thompson, E. Quataert, D. Zhang, D. H. Weinberg, An origin for multiphase gas in galactic winds and haloes. *Mon. Not. R. Astron. Soc.* **455** (2), 1830–1844 (2016), doi:10.1093/mnras/stv2428.
3. S. Veilleux, G. Cecil, J. Bland-Hawthorn, Galactic Winds. *Annu. Rev. Astron. Astrophys.* **43** (1), 769–826 (2005), doi:10.1146/annurev.astro.43.072103.150610.
4. S. Veilleux, R. Maiolino, A. D. Bolatto, S. Aalto, Cool outflows in galaxies and their implications. *Astron. Astrophys. Rev.* **28** (1), 2 (2020), doi:10.1007/s00159-019-0121-9.
5. T. A. Thompson, T. M. Heckman, Theory and Observation of Winds from Star-Forming Galaxies. *Annu. Rev. Astron. Astrophys.* **62** (1), 529–591 (2024), doi:10.1146/annurev-astro-041224-011924.
6. P. S. Behroozi, C. Conroy, R. H. Wechsler, A Comprehensive Analysis of Uncertainties Affecting the Stellar Mass-Halo Mass Relation for $0 < z < 4$. *Astrophys. J.* **717** (1), 379–403 (2010), doi:10.1088/0004-637X/717/1/379.
7. B. P. Moster, T. Naab, S. D. M. White, Galactic star formation and accretion histories from matching galaxies to dark matter haloes. *Mon. Not. R. Astron. Soc.* **428** (4), 3121–3138 (2013), doi:10.1093/mnras/sts261.
8. E. Puchwein, V. Springel, Shaping the galaxy stellar mass function with supernova- and AGN-driven winds. *Mon. Not. R. Astron. Soc.* **428** (4), 2966–2979 (2013), doi:10.1093/mnras/sts243.
9. M. Vogelsberger, F. Marinacci, P. Torrey, E. Puchwein, Cosmological simulations of galaxy formation. *Nature Reviews Physics* **2** (1), 42–66 (2020), doi:10.1038/s42254-019-0127-2.

10. P. F. Hopkins, *et al.*, Galaxies on FIRE (Feedback In Realistic Environments): stellar feedback explains cosmologically inefficient star formation. *Mon. Not. R. Astron. Soc.* **445** (1), 581–603 (2014), doi:10.1093/mnras/stu1738.
11. P. F. Hopkins, *et al.*, FIRE-2 simulations: physics versus numerics in galaxy formation. *Mon. Not. R. Astron. Soc.* **480** (1), 800–863 (2018), doi:10.1093/mnras/sty1690.
12. J. Schaye, *et al.*, The EAGLE project: simulating the evolution and assembly of galaxies and their environments. *Mon. Not. R. Astron. Soc.* **446** (1), 521–554 (2015), doi:10.1093/mnras/stu2058.
13. M. Vogelsberger, *et al.*, Introducing the Illustris Project: simulating the coevolution of dark and visible matter in the Universe. *Mon. Not. R. Astron. Soc.* **444** (2), 1518–1547 (2014), doi:10.1093/mnras/stu1536.
14. D. Nelson, *et al.*, The illustris simulation: Public data release. *Astronomy and Computing* **13**, 12–37 (2015), doi:10.1016/j.ascom.2015.09.003.
15. DESI Collaboration, *et al.*, The Early Data Release of the Dark Energy Spectroscopic Instrument. *Astron. J.* **168** (2), 58 (2024), doi:10.3847/1538-3881/ad3217.
16. J. Brinchmann, *et al.*, The physical properties of star-forming galaxies in the low-redshift Universe. *Mon. Not. R. Astron. Soc.* **351** (4), 1151–1179 (2004), doi:10.1111/j.1365-2966.2004.07881.x.
17. K. G. Noeske, *et al.*, Star Formation in AEGIS Field Galaxies since $z=1.1$: Staged Galaxy Formation and a Model of Mass-dependent Gas Exhaustion. *Astrophys. J. Lett.* **660** (1), L47–L50 (2007), doi:10.1086/517927.
18. J. S. Speagle, C. L. Steinhardt, P. L. Capak, J. D. Silverman, A Highly Consistent Framework for the Evolution of the Star-Forming “Main Sequence” from $z \sim 0$ –6. *Astrophys. J. Suppl. Ser.* **214** (2), 15 (2014), doi:10.1088/0067-0049/214/2/15.
19. R. Bordoloi, *et al.*, The Dependence of Galactic Outflows on the Properties and Orientation of zCOSMOS Galaxies at $z \sim 1$. *Astrophys. J.* **794** (2), 130 (2014), doi:10.1088/0004-637X/794/2/130.

20. Materials and methods are available as supplementary material.
21. T.-W. Lan, M. Fukugita, Mg II Absorbers: Metallicity Evolution and Cloud Morphology. *Astrophys. J.* **850** (2), 156 (2017), doi:10.3847/1538-4357/aa93eb.
22. P. D. Mitchell, J. Schaye, R. G. Bower, R. A. Crain, Galactic outflow rates in the EAGLE simulations. *Mon. Not. R. Astron. Soc.* **494** (3), 3971–3997 (2020), doi:10.1093/mnras/staa938.
23. K. H. R. Rubin, *et al.*, Evidence for Ubiquitous Collimated Galactic-scale Outflows along the Star-forming Sequence at $z \sim 0.5$. *Astrophys. J.* **794** (2), 156 (2014), doi:10.1088/0004-637X/794/2/156.
24. B. J. Weiner, *et al.*, Ubiquitous Outflows in DEEP2 Spectra of Star-Forming Galaxies at $z = 1.4$. *Astrophys. J.* **692** (1), 187–211 (2009), doi:10.1088/0004-637X/692/1/187.
25. J. Chisholm, C. A. Tremonti, C. Leitherer, Y. Chen, The mass and momentum outflow rates of photoionized galactic outflows. *Mon. Not. R. Astron. Soc.* **469** (4), 4831–4849 (2017), doi:10.1093/mnras/stx1164.
26. A. M. Swinbank, *et al.*, The energetics of starburst-driven outflows at $z \sim 1$ from KMOS. *Mon. Not. R. Astron. Soc.* **487** (1), 381–393 (2019), doi:10.1093/mnras/stz1275.
27. X. Xu, *et al.*, CLASSY III. The Properties of Starburst-driven Warm Ionized Outflows. *Astrophys. J.* **933** (2), 222 (2022), doi:10.3847/1538-4357/ac6d56.
28. C. R. Avery, *et al.*, Cool outflows in MaNGA: a systematic study and comparison to the warm phase. *Mon. Not. R. Astron. Soc.* **511** (3), 4223–4237 (2022), doi:10.1093/mnras/stac190.
29. C. Leitherer, *et al.*, Starburst99: Synthesis Models for Galaxies with Active Star Formation. *Astrophys. J. Suppl. Ser.* **123** (1), 3–40 (1999), doi:10.1086/313233.
30. N. Murray, E. Quataert, T. A. Thompson, On the Maximum Luminosity of Galaxies and Their Central Black Holes: Feedback from Momentum-driven Winds. *Astrophys. J.* **618** (2), 569–585 (2005), doi:10.1086/426067.
31. J. Buchner, Nested Sampling Methods. *Statistics Surveys* **17**, 169–215 (2023), doi:10.1214/23-SS144.

32. J. F. Navarro, C. S. Frenk, S. D. M. White, The Structure of Cold Dark Matter Halos. *Astrophys. J.* **462**, 563 (1996), doi:10.1086/177173.
33. M. Miyamoto, R. Nagai, Three-dimensional models for the distribution of mass in galaxies. *Publ. Astron. Soc. Jpn* **27**, 533–543 (1975).
34. Z. Chen, *et al.*, The Circumgalactic Medium Traced by Mg II Absorption with DESI: Dependence on Galaxy Stellar Mass, Star Formation Rate, and Azimuthal Angle. *Astrophys. J.* **981** (1), 81 (2025), doi:10.3847/1538-4357/ada942.
35. Y. Guo, *et al.*, Bipolar outflows out to 10 kpc for massive galaxies at redshift $z \approx 1$. *Nature* **624** (7990), 53–56 (2023), doi:10.1038/s41586-023-06718-w.
36. C. W. Trapp, *et al.*, Gas infall and radial transport in cosmological simulations of milky way-mass discs. *Mon. Not. R. Astron. Soc.* **509** (3), 4149–4170 (2022), doi:10.1093/mnras/stab3251.
37. S. S. McGaugh, J. M. Schombert, W. J. G. de Blok, M. J. Zagursky, The Baryon Content of Cosmic Structures. *Astrophys. J. Lett.* **708** (1), L14–L17 (2010), doi:10.1088/2041-8205/708/1/L14.
38. DESI Collaboration, *et al.*, DESI 2024 II: Sample Definitions, Characteristics, and Two-point Clustering Statistics. *arXiv e-prints* arXiv:2411.12020 (2024), doi:10.48550/arXiv.2411.12020.
39. DESI Collaboration, *et al.*, Overview of the Instrumentation for the Dark Energy Spectroscopic Instrument. *Astron. J.* **164** (5), 207 (2022), doi:10.3847/1538-3881/ac882b.
40. M. Boquien, *et al.*, CIGALE: a python Code Investigating GALaxy Emission. *Astron. Astrophys.* **622**, A103 (2019), doi:10.1051/0004-6361/201834156.
41. G. Yang, *et al.*, X-CIGALE: Fitting AGN/galaxy SEDs from X-ray to infrared. *Mon. Not. R. Astron. Soc.* **491** (1), 740–757 (2020), doi:10.1093/mnras/stz3001.
42. G. Yang, *et al.*, Fitting AGN/Galaxy X-Ray-to-radio SEDs with CIGALE and Improvement of the Code. *Astrophys. J.* **927** (2), 192 (2022), doi:10.3847/1538-4357/ac4971.

43. H. Zou, *et al.*, A Large Sample of Extremely Metal-poor Galaxies at $z \lesssim 1$ Identified from the DESI Early Data. *Astrophys. J.* **961** (2), 173 (2024), doi:10.3847/1538-4357/ad1409.
44. I. Schroetter, *et al.*, MusE GAs FLOW and Wind (MEGAFLOW) - III. Galactic wind properties using background quasars. *Mon. Not. R. Astron. Soc.* **490** (3), 4368–4381 (2019), doi:10.1093/mnras/stz2822.
45. D. J. Schlegel, D. P. Finkbeiner, M. Davis, Maps of Dust Infrared Emission for Use in Estimation of Reddening and Cosmic Microwave Background Radiation Foregrounds. *Astrophys. J.* **500** (2), 525–553 (1998), doi:10.1086/305772.
46. T. Garn, P. N. Best, Predicting dust extinction from the stellar mass of a galaxy. *Mon. Not. R. Astron. Soc.* **409** (1), 421–432 (2010), doi:10.1111/j.1365-2966.2010.17321.x.
47. G. Chabrier, Galactic Stellar and Substellar Initial Mass Function. *Publ. Astron. Soc. Pac.* **115** (809), 763–795 (2003), doi:10.1086/376392.
48. D. Calzetti, *et al.*, The Dust Content and Opacity of Actively Star-forming Galaxies. *Astrophys. J.* **533** (2), 682–695 (2000), doi:10.1086/308692.
49. A. C. Carnall, SpectRes: A Fast Spectral Resampling Tool in Python. *arXiv e-prints* arXiv:1705.05165 (2017), doi:10.48550/arXiv.1705.05165.
50. G. B. Zhu, *et al.*, Near-ultraviolet Spectroscopy of Star-forming Galaxies from eBOSS: Signatures of Ubiquitous Galactic-scale Outflows. *Astrophys. J.* **815** (1), 48 (2015), doi:10.1088/0004-637X/815/1/48.
51. K. H. R. Rubin, *et al.*, The Persistence of Cool Galactic Winds in High Stellar Mass Galaxies between $z \sim 1.4$ and ~ 1 . *Astrophys. J.* **719** (2), 1503–1525 (2010), doi:10.1088/0004-637X/719/2/1503.
52. Y.-M. Chen, *et al.*, Absorption-line Probes of the Prevalence and Properties of Outflows in Present-day Star-forming Galaxies. *Astron. J.* **140** (2), 445–461 (2010), doi:10.1088/0004-6256/140/2/445.

53. C. L. Martin, *et al.*, Demographics and Physical Properties of Gas Outflows/Inflows at $0.4 < z < 1.4$. *Astrophys. J.* **760** (2), 127 (2012), doi:10.1088/0004-637X/760/2/127.
54. D. K. Erb, A. M. Quider, A. L. Henry, C. L. Martin, Galactic Outflows in Absorption and Emission: Near-ultraviolet Spectroscopy of Galaxies at $1 < z < 2$. *Astrophys. J.* **759** (1), 26 (2012), doi:10.1088/0004-637X/759/1/26.
55. J. N. Burchett, *et al.*, Circumgalactic Mg II Emission from an Isotropic Starburst Galaxy Outflow Mapped by KCWI. *Astrophys. J.* **909** (2), 151 (2021), doi:10.3847/1538-4357/abd4e0.
56. I. Pessa, *et al.*, A galactic outflow traced by its extended Mg II emission out to a ~ 30 kpc radius in the Hubble Ultra Deep Field with MUSE. *Astron. Astrophys.* **691**, A5 (2024), doi:10.1051/0004-6361/202450547.
57. B. P. Moster, *et al.*, Constraints on the Relationship between Stellar Mass and Halo Mass at Low and High Redshift. *Astrophys. J.* **710** (2), 903–923 (2010), doi:10.1088/0004-637X/710/2/903.
58. A. V. Macciò, *et al.*, Concentration, spin and shape of dark matter haloes: scatter and the dependence on mass and environment. *Mon. Not. R. Astron. Soc.* **378** (1), 55–71 (2007), doi:10.1111/j.1365-2966.2007.11720.x.
59. H. Guo, Y. Shen, S. Wang, PyQSOFit: Python code to fit the spectrum of quasars, Astrophysics Source Code Library, record ascl:1809.008 (2018).
60. S. Perrotta, *et al.*, Kinematics, Structure, and Mass Outflow Rates of Extreme Starburst Galactic Outflows. *Astrophys. J.* **949** (1), 9 (2023), doi:10.3847/1538-4357/acc660.
61. B. Reichardt Chu, *et al.*, DUVET: sub-kiloparsec resolved star formation driven outflows in a sample of local starbursting disc galaxies. *Mon. Not. R. Astron. Soc.* **536** (2), 1799–1821 (2025), doi:10.1093/mnras/stae2705.
62. D. Nelson, *et al.*, First results from the TNG50 simulation: galactic outflows driven by supernovae and black hole feedback. *Mon. Not. R. Astron. Soc.* **490** (3), 3234–3261 (2019), doi:10.1093/mnras/stz2306.

63. D. Anglés-Alcázar, *et al.*, The cosmic baryon cycle and galaxy mass assembly in the FIRE simulations. *Mon. Not. R. Astron. Soc.* **470** (4), 4698–4719 (2017), doi:10.1093/mnras/stx1517.
64. V. Pandya, *et al.*, Characterizing mass, momentum, energy, and metal outflow rates of multiphase galactic winds in the FIRE-2 cosmological simulations. *Mon. Not. R. Astron. Soc.* **508** (2), 2979–3008 (2021), doi:10.1093/mnras/stab2714.
65. S. Juneau, M. Dickinson, D. M. Alexander, S. Salim, A New Diagnostic of Active Galactic Nuclei: Revealing Highly Absorbed Systems at Redshift $z < 0.3$. *Astrophys. J.* **736** (2), 104 (2011), doi:10.1088/0004-637X/736/2/104.
66. S. Juneau, *et al.*, Active Galactic Nuclei Emission Line Diagnostics and the Mass-Metallicity Relation up to Redshift $z \sim 2$: The Impact of Selection Effects and Evolution. *Astrophys. J.* **788** (1), 88 (2014), doi:10.1088/0004-637X/788/1/88.
67. R. Pucha, *et al.*, Tripling the Census of Dwarf AGN Candidates Using DESI Early Data. *arXiv e-prints* arXiv:2411.00091 (2024), doi:10.48550/arXiv.2411.00091.

Acknowledgments

Funding: The authors are supported by the National Key R&D Program of China (grant Nos. 2022YFA1602902 and 2023YFA1607804) and the National Natural Science Foundation of China (NSFC; grant Nos. 12473008, 12192224, 12120101003 and 12373010). The authors gratefully acknowledge the support of Cyrus Chun Ying Tang Foundations and CAS Project for Young Scientists in Basic Research, Grant No. YSBR-062.

Author contributions: E. W. proposed and developed the idea. H. Y. did the primary data analysis. Z. C. calculated the star formation rates from emission lines, and analyzed the CGM absorption using background quasars. H. Y. plotted the figures and wrote the manuscript. E. W. revised the manuscript. All authors participated in discussion and helped to shape the manuscript.

Competing interests: There are no competing interests to declare.

Supplementary materials

Materials and Methods

Figs. S1 to S7

References (38-67)

Supplementary Materials for
Stellar feedback drives the baryon deficiency in low-mass
galaxies

Haoran Yu, Enci Wang*, Zeyu Chen, Céline Péroux,
Hu Zou, Zhicheng He, Huiyuan Wang, Cheqiu Lyu,
Cheng Jia, Chengyu Ma, Xu Kong

*Corresponding author. Email: ecwang16@ustc.edu.cn

This PDF file includes:

Materials and Methods

Figures S1 to S7

Materials and Methods

Sample selection

Our sample is drawn from ELGs in DESI EDR (38). We implement a redshift cut of $z > 0.3$ to ensure spectral coverage of the Mg II $\lambda\lambda$ 2796,2803 doublet. Considering the low S/N in the blue-tail of DESI spectra which is compromised by the low transmission in the blue spectrograph (39), we further restrict the sample to $z > 0.6$. The stellar mass of each galaxy is estimated through stellar population synthesis fitting using Code Investigating GALaxy Emission (CIGALE) (40–42), which utilizes the broad-band g , r , z , $W1$ and $W2$ photometry from the DESI Legacy Imaging Surveys, and spectrophotometry of 10 artificial bands via convolution with the DESI optical spectra (43). The star formation rates are estimated based on the flux of [O II] $\lambda\lambda$ 3726,3729 emission line (44), using the relation

$$\frac{\text{SFR}(\text{O II})}{\text{M}_{\odot} \text{ yr}^{-1}} = 4.1 \times 10^{-42} \frac{L(\text{O II})}{\text{erg s}^{-1}}, \quad (\text{S1})$$

where the luminosity has been corrected for both Milky Way extinction (45) and the intrinsic galaxy extinction (46), assuming the Chabrier initial mass function (47) and Calzetti extinction law (48).

We apply the following selection criteria to the ELGs: (i) The uncertainty in M_* is less than 0.3 dex, ensuring reliable mass measurements; (ii) $10^6 \text{ M}_{\odot} < M_* < 10^{14} \text{ M}_{\odot}$ and $10^{-4} \text{ M}_{\odot} \text{ yr}^{-1} < \text{SFR} < 10^4 \text{ M}_{\odot} \text{ yr}^{-1}$, excluding unphysical outliers. After applying the cuts, our final sample comprises 394,909 ELGs spanning $0.6 < z < 1.7$, with median stellar mass of $10^{9.8} \text{ M}_{\odot}$ and median SFR of $11.8 \text{ M}_{\odot} \text{ yr}^{-1}$. The distributions of M_* , SFR and z are illustrated in Figure S1.

Spectral Stacking

We begin by shifting all individual spectra to rest-frame wavelengths and resampling them onto a common grid with a 0.6 \AA wavelength interval using SPECTRES (49). Following this, a median filter with a smoothing window of 60 \AA is applied before a fifth-order polynomial is fitted to the smoothed spectrum, deriving the continuum for the individual galaxy spectrum. Throughout the aforementioned process, the prominent absorption and emission lines are masked: (i) $\pm 20 \text{ \AA}$ around Mg II $\lambda\lambda$ 2796,2803; (ii) $\pm 10 \text{ \AA}$ around Mg I λ 2851 and (iii) $\pm 40 \text{ \AA}$ around Fe II λ 2600. We then obtain the stacked spectra by calculating the median of the continuum-normalized spectra

in different sample bins. Focusing on the outflow features in the $\text{Mg II } \lambda\lambda 2796, 2803$ absorption profile, we have examined that most stacked spectra show flat continuum outside the absorption troughs. However, at high mass end, a few stacked spectra exhibit continuum elevations around Mg II absorptions up to $\sim 10\%$ above unity, extending out to $\sim 2000 \text{ km s}^{-1}$. This phenomenon may arise from the inclusion of AGNs producing broad Mg II emission lines, which could affect the measurements of the outflow properties for the most massive galaxy bins. We therefore perform another normalization to the stacked spectra to remove this large-scale residual, by dividing a triple-order polynomial fitting of the continuum while masking out $2785\text{--}2810 \text{ \AA}$ (50). For consistency, all stacked spectra are re-normalized. We quantify uncertainties in the stacked spectra using bootstrap resampling: the stacking procedure is repeated 1,000 times with replacement, with the 16–84th percentile range of the bootstrap realizations defining the 1σ confidence interval for each spectral bin. The stacked spectra corresponding to the bins in Figure 2 of the main part are shown in Figure S2. All stacked spectra exhibit overall blue-shifted Mg II absorption, which is a hallmark of galactic-scale outflows. The level of scattered emission increases as the stellar mass decreases, resulting in the P-Cygni profile (51–56). The outflow properties are extracted based on these stacked spectra in this work.

Outflow Properties

Considering the insufficient spectral resolution of the stacked spectra to resolve absorption of different optical depths, we determine the outflow properties from the composite spectra through the `BOXCAR` method (19, 51), as illustrated in Figure S3. In this method, we neglect the spectral range between the Mg II doublet and only consider -700 to 0 km s^{-1} relative to $\text{Mg II } \lambda 2796$ and 0 to 400 km s^{-1} relative to $\text{Mg II } \lambda 2803$. We then derive outflow EW through subtracting the non-outflowing symmetrical component (indicated by the orange band) from the total absorption (indicated by the blue band). Although `BOXCAR` method overlooks the complicated radiative transfer processes in the outflows, it is nearly model-independent, which can directly extract the outflow features from the observed absorption profile. This is favored in our statistical analysis of a large sample, highlighting the different outflow properties of various galaxy populations.

We calculate the EW of the blue-shifted absorption relative to $\text{Mg II } \lambda 2796$ and the red-shifted

profile relative to Mg II $\lambda 2803$ as EW_{blue} and EW_{red} , based on the two aforementioned wavelength intervals. For simplicity, we decompose the absorption profile into two components: an outflowing component (out), characterized by a blue-shifted line center, and an interstellar component (sym), with a symmetric profile centered at the rest-frame wavelength. Ignoring the mixed absorption and emission between 2796 Å and 2803 Å, the total equivalent width of the doublet defined as $EW_{\text{tot}} \equiv EW_{\text{out}} + EW_{\text{sym}}$ and the equivalent width of the outflowing component EW_{out} are estimated as

$$EW_{\text{tot}} = 2(EW_{\text{blue}} + EW_{\text{red}}), \quad (\text{S2})$$

$$EW_{\text{out}} = 2(EW_{\text{blue}} - EW_{\text{red}}). \quad (\text{S3})$$

Figure S4 presents the measured EW_{out} as functions of M_* and SFR, together with results from previous Mg II absorption stacking studies (19, 24, 51) for comparison. We note that older studies observed weak positive correlation between EW_{out} and $\log M_*$, whereas our data reveals that EW_{out} remains almost constant in a given redshift bin. On the other hand we observe positive $EW_{\text{out}} - \log \text{SFR}$ correlation in each redshift bin, which is consistent with those studies. This implicates that the $EW_{\text{out}} - \log M_*$ relation is a byproduct of the strong $M_* - z$ relation, strengthening that outflows vary with star-formation rates within galaxies which evolves through the cosmic time.

The EW-weighted mean velocity of the total absorption can be calculated as v_{tot} . Considering that the velocity of the symmetric component is 0, the velocity of the outflowing component is calculated as

$$v_{\text{out}} = \frac{EW_{\text{tot}}}{EW_{\text{out}}} \cdot v_{\text{tot}}. \quad (\text{S4})$$

We then adopt an empirical linear relation to convert $EW(\text{Mg II})$ into the column density of neutral Hydrogen (21), as

$$N_{\text{HI}} = A \left(\frac{EW_{\lambda 2796}}{1 \text{ Å}} \right)^\alpha (1+z)^\beta \quad (\text{S5})$$

where $\alpha = 1.69 \pm 0.13$, $\beta = 1.88 \pm 0.29$ and $A = 10^{18.96 \pm 0.10} \text{ cm}^{-2}$. The $EW_{\lambda 2796}$ is the equivalent width of Mg II $\lambda 2796$ absorption, which we assume to be half of the total doublet EW. The mass outflow rate is then calculated assuming the geometry of the outflow to be an expanding thin spherical shell (24):

$$\dot{M}_{\text{out}} = 22 M_\odot \text{ yr}^{-1} \cdot C_f \cdot \frac{N_{\text{HI}}}{1 \times 10^{20} \text{ cm}^{-2}} \cdot \frac{r}{r_{\text{launch}}} \cdot \frac{v_{\text{out}}}{300 \text{ km s}^{-1}}, \quad (\text{S6})$$

where C_f is the cover fraction of the outflow which we assume to be 0.9. The launch radius r_{launch} must be at least of the order of the galaxy radius (24), which is poorly constrained for our $z > 0.6$ sample because of the low spatial resolution of DESI legacy imaging surveys. Here we assume the launch radius of the outflow is fixed at $r_{\text{launch}} = 5 \text{ kpc}$ for simplicity. From this equation, \dot{M}_{out} is proportional to the production of v_{out} and a power of EW_{out} .

The uncertainties in EW_{out} and v_{out} are quantified through an analysis of 1,000 stacked spectra generated via bootstrap resamplings. We apply the `Boxcar` method on these resampled spectra and determine the 1σ confidence intervals for EW_{out} and v_{out} by calculating the 16-84th percentile ranges of the bootstrap distributions. The uncertainties in the empirical relations (Equation S5) are considered when calculating the uncertainty in \dot{M}_{out} . The uncertainty in η is further derived using error propagation, assuming that the uncertainties in the SFR measurements are negligible.

Gravity Potential Modelling

We determine the mass of dark matter halos (DMHs) corresponding to different stellar mass through the M_* - M_{halo} relation from Moster et al. (57), and assume an NFW density profile (32) which is expressed as

$$\frac{\rho(r)}{\rho_{\text{crit}}} = \frac{\delta_c}{(r/r_s)(1 + r/r_s)^2}, \quad (\text{S7})$$

where $r_s = r_{200}/c$ is a characteristic radius and $\rho_{\text{crit}} = 3H^2/8\pi G$. δ_c is a dimensionless parameter defined as

$$\delta_c = \frac{200}{3} \frac{c^3}{[\ln(1 + c) - c/(1 + c)]}, \quad (\text{S8})$$

where c is the concentration parameter depending on M_{halo} , which is taken from Equation 8 from Maccio et al. 2007 (58). By integrating the density profile, we obtain the gravity potential of an NFW halo as

$$\Phi_{\text{NFW}}(r) = -4\pi G \rho_{\text{crit}} \delta_c r_s^3 \frac{1}{r + r_s}. \quad (\text{S9})$$

Additionally, we consider the potential of an exponential disk (33) in the form of

$$\Phi_{\text{disk}}(R, z) = \frac{GM}{\{R^2 + [a + (z^2 + b^2)^{1/2}]^2\}^{1/2}}, \quad (\text{S10})$$

where we assume $a = 3 \text{ kpc}$, $b = 0.3 \text{ kpc}$ and $R = 0$, considering the physical size of our sample is comparable to 3 kpc. The total gravity potential is obtained through summing Φ_{NFW} and Φ_{disk} .

Mg II Absorption in the CGM

As demonstrated in the main text, we find that outflow velocities decline rapidly as they propagate in massive galaxies ($M_* > 10^{10} M_\odot$). This behavior may leave a distinct imprint on the metal distribution within the CGM, potentially differentiating low- and high-mass galaxies. To explore this further, we analyze EW(Mg II) in the CGM using stacked background quasar spectra. The methodology for this CGM analysis differs somewhat from the approach adopted in our primary study, as summarized below (see Chen et al. (34) for a comprehensive description).

Using the DESI EDR catalog, we identify quasar-galaxy pairs by cross-matching their coordinates and selecting those with a projected impact parameter of < 150 kpc. To mitigate contamination from quasar-associated absorption features, we require that the quasar redshifts exceed those of the foreground galaxies by $\Delta z > 0.02$. We first fit the intrinsic quasar spectra using PyQSOFit (59) for each individual spectrum. The observed spectra are then normalized by dividing them by their best-fit quasar model spectrum. To further suppress high-frequency noise, we apply a median filter to the normalized spectra, excluding the wavelength regions containing Mg II absorption to avoid biasing the smoothing process. Finally, we stack the processed spectra in the rest-frame of the foreground galaxies, generating a composite spectrum by taking the median flux at each wavelength.

The stacked Mg II absorption spectra of the CGM are shown in Figure S5, which corresponds to the data points in the bottom panel of Figure 4 in the main text. To quantify the absorption strength, we model the Mg II doublet using a double-Gaussian profile and calculate the equivalent width by integrating the absorption flux over a 3σ wavelength window centered on the best-fit model. Uncertainties in the EW measurements are derived from 100 bootstrap iterations.

The Mass-Loading Factor

While the hot gas in the CGM occupies large fraction of volume, the cool, neutral phase gas ($\sim 10^4$ K) traced by Mg II could dominate the mass of outflows, which is physically important. We compare the mass-loading factor derived in this work with results from multiple hydrodynamical simulations in Figure S6. Additionally, we include results from recent observations, encompassing studies based on CGM metal absorption (44), “down-the-barrel” metal absorption (60), and emission measurements (61). Our derived mass-loading factor decreases as the stellar mass increases, which

agrees with the predictions from those simulations. Compared with Illustris (14), IllustrisTNG (62) and FIRE (63), our data show similar slope but is lower by 0.5-1.0 dex. η from EAGLE (22) is close to our estimates for $M_* \lesssim 10^{9.5} M_\odot$ galaxies, but deviates towards higher values for massive systems, which could be an effect of the AGN feedback implemented in the simulation. However, we note several caveats in calculating the outflow rate, including the assumed relation between $\text{EW}_{\lambda 2796}$ and N_{HI} , the simplified geometry and metallicity of the outflowing gas. These parameter assumptions introduce systematic error in estimating the mass loading factor, making comparison between different works difficult. Note that the physical conditions adopted by different simulations varies to some extent. While in IllustrisTNG the mass loading is calculated at the self-prescribed injection scale (62), in FIRE it is estimated by fitting particle-tracking based measurements (64), and EAGLE considers mass loading on ISM scale. In down-the-barrel observations, the actual launch radii of the outflows are difficult to constrain. We note that a persistent tension remains between the state-of-the-art simulations and observations, highlighting the need for further efforts to reconcile the two from both sides.

Active Galactic Nuclei Contamination

While this study does not a priori exclude AGN contributions in spectral stacking, we explicitly evaluate their potential influence in this section. Given the lack of $\text{H}\alpha$ and $[\text{NII}]\lambda 6583$ emission measurements for the majority of our sample, we employ the “Mass-Excitation” (MEx) diagnostic diagram (65, 66) to identify AGNs. We focus on the subset of galaxies with $z < 1$ where $\text{H}\beta$ and $[\text{OIII}]\lambda 5007$ emission lines are accessible. By applying SNR thresholds of $\text{SNR}(\text{H}\beta) > 5$ and $\text{SNR}([\text{OIII}]\lambda 5007) > 10$, we retain 40,079 galaxies, with 7,114 (17.7% of this subset) classified as AGNs. As the decline in AGN prevalence with redshift for low-mass galaxies has been observed (67), the AGN fraction in higher-redshift ($z > 1$) galaxies is likely no larger than this value.

Panel A of Figure S7 shows the classification of AGNs using the $[\text{OIII}]/\text{H}\beta$ flux ratio versus stellar mass diagram. In the MEx diagram, the main empirical division is defined as follows:

$$y = \begin{cases} 0.37/(x - 10.5) + 1 & \text{if } x \leq 9.9, \\ 594.753 - 167.074x + 15.6748x^2 - 0.491215x^3 & \text{otherwise.} \end{cases} \quad (\text{S11})$$

We then examine whether the outflow properties vary significantly with or without AGNs. The

results are shown in the panel B and C of Figure S7. Following the spectral stacking methodology applied in Figure 2, we sort the sample by stellar mass and generate stacked spectra for bins of 5,000 galaxies each. We find that including AGNs results in slight variation in v_{out} and EW_{out} of less than 5%. However, at $M_* \sim 10^{10} M_{\odot}$, excluding potential AGNs leads to an increase of EW_{out} of $\sim 10\%$, resulting in a weak positive correlation between EW_{out} and $\log M_*$. This may be due to the contribution of broad Mg II emission lines from AGNs, which can dilute absorption features in the median-stacking analysis. Consequently, the values of EW_{out} , \dot{M}_{out} and η at $M_* \gtrsim 10^{10} M_{\odot}$ could be underestimated to some extent, which should be treated with caution.

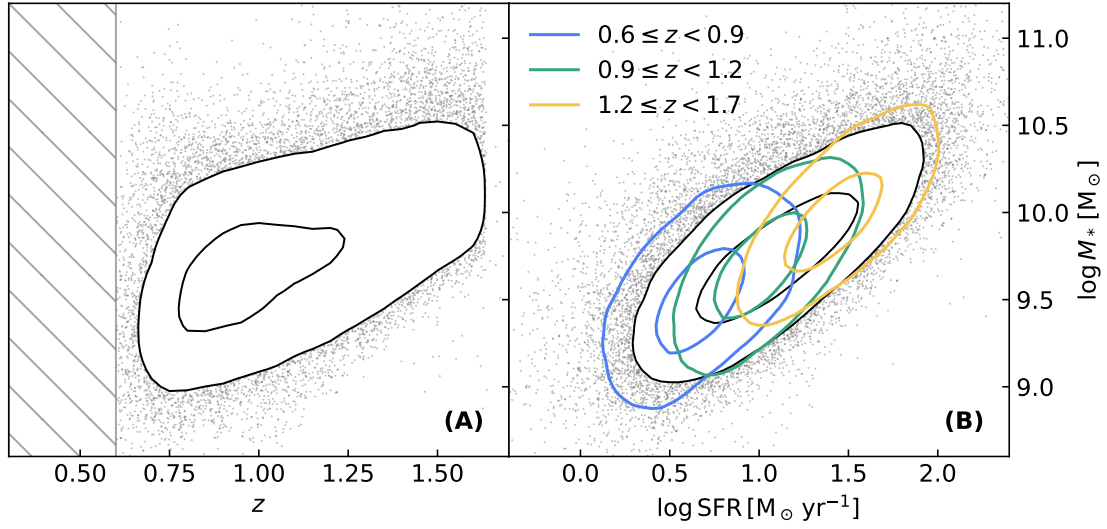


Figure S1: Sample parameter distribution. (A) $\log M_*$ - z distribution. The inner and outer black contours enclose 68% and 95% of the sample, respectively. For visual clarity, only 10% of the points falling outside the outer contour are plotted. (B) $\log M_*$ - $\log \text{SFR}$ distribution. The blue, green and yellow contours indicate the distribution of samples with $0.6 < z < 0.9$, $0.9 < z < 1.2$ and $1.2 < z < 1.7$, respectively. Similar to the black contours, these enclose 68% and 95% of the corresponding redshift subsamples.

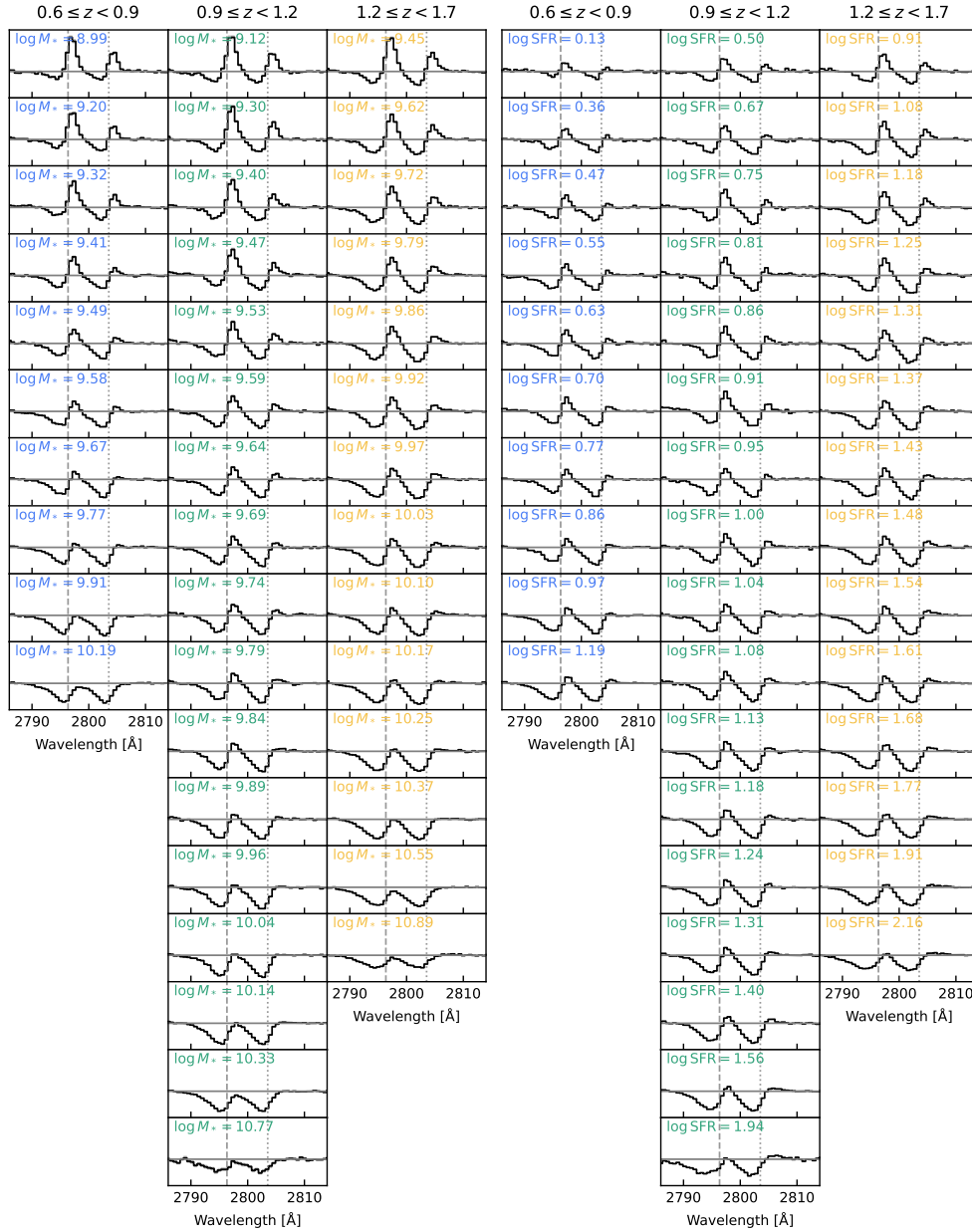


Figure S2: The stacked galaxy spectra in bins of M_* and SFR. Each spectrum is derived by stacking 10,000 spectra, corresponding to the data points in Figure 2 in the main part. The left group of panels show the spectra in bins of M_* , with increasing M_* from top to bottom, while the right group of panels show the spectra in bins of SFR. Blue, green and yellow represents samples with $0.6 \leq z < 0.9$, $0.9 \leq z < 1.2$ and $1.2 \leq z < 1.7$, respectively. The uncertainties of the spectra are small thus are not presented.

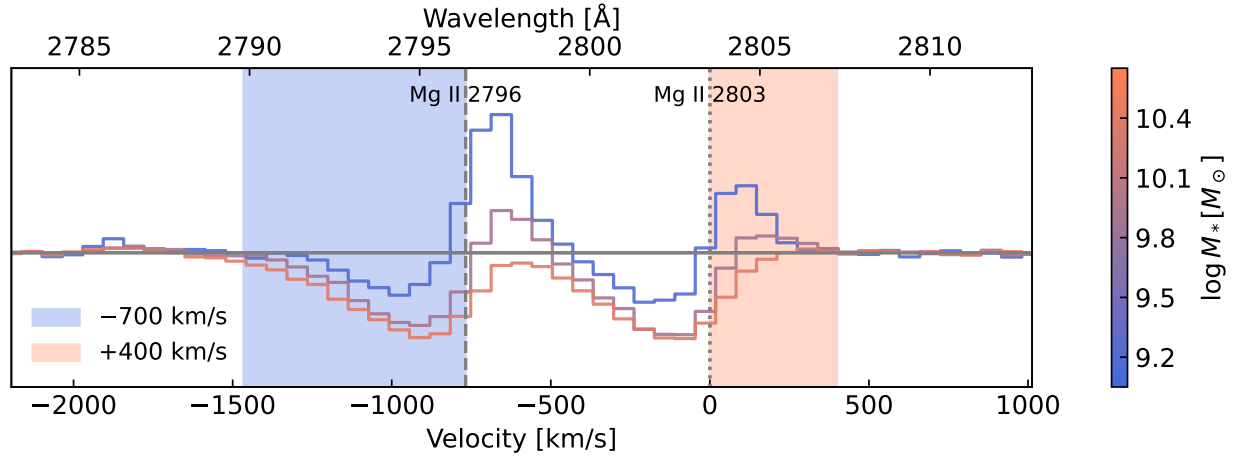


Figure S3: Illustration of the BoxCAR method for measuring outflow properties on the stacked spectra. The color of the curves corresponds to M_* of the galaxies. The dashed and dotted lines indicate the rest-frame wavelengths of Mg II $\lambda 2796$ and Mg II $\lambda 2803$, respectively. All composite spectra presented here are obtained by stacking 20,000 individual galaxy spectra. The blue and orange shaded regions correspond to velocity range of -700 to 0 km s^{-1} relative to Mg II $\lambda 2796$ and 0 to 400 km s^{-1} relative to Mg II $\lambda 2803$, respectively. These two wavelength intervals are used to calculate outflow properties throughout this work. Labels at the top of the figure indicate the rest-frame wavelengths, while those at the bottom show velocities relative to Mg II $\lambda 2803$.

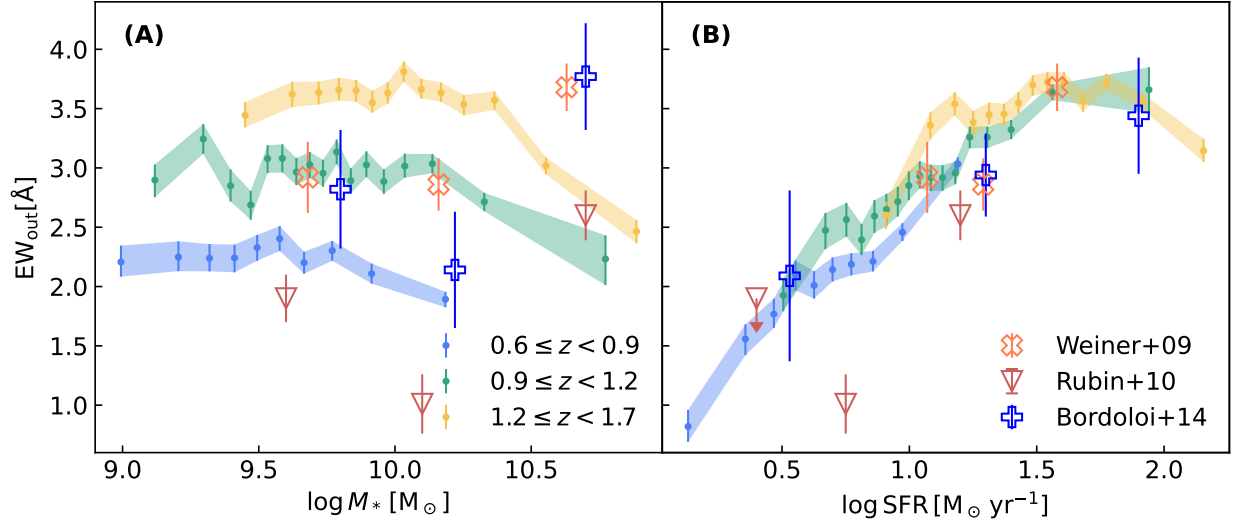


Figure S4: EW_{out} measurements in comparison with previous studies. (A) The measured outflow equivalent width (EW_{out}) in $\log M_*$ bins. The data points colored by redshift represent the same bins as those shown in Figure 2 in the main part. The outflow EW is estimated using Equation S3. (B) The measured outflow equivalent width (EW_{out}) in $\log \text{SFR}$ bins. The open symbols represent outflow EW measurements obtained from the literature, as indicated in the legend.

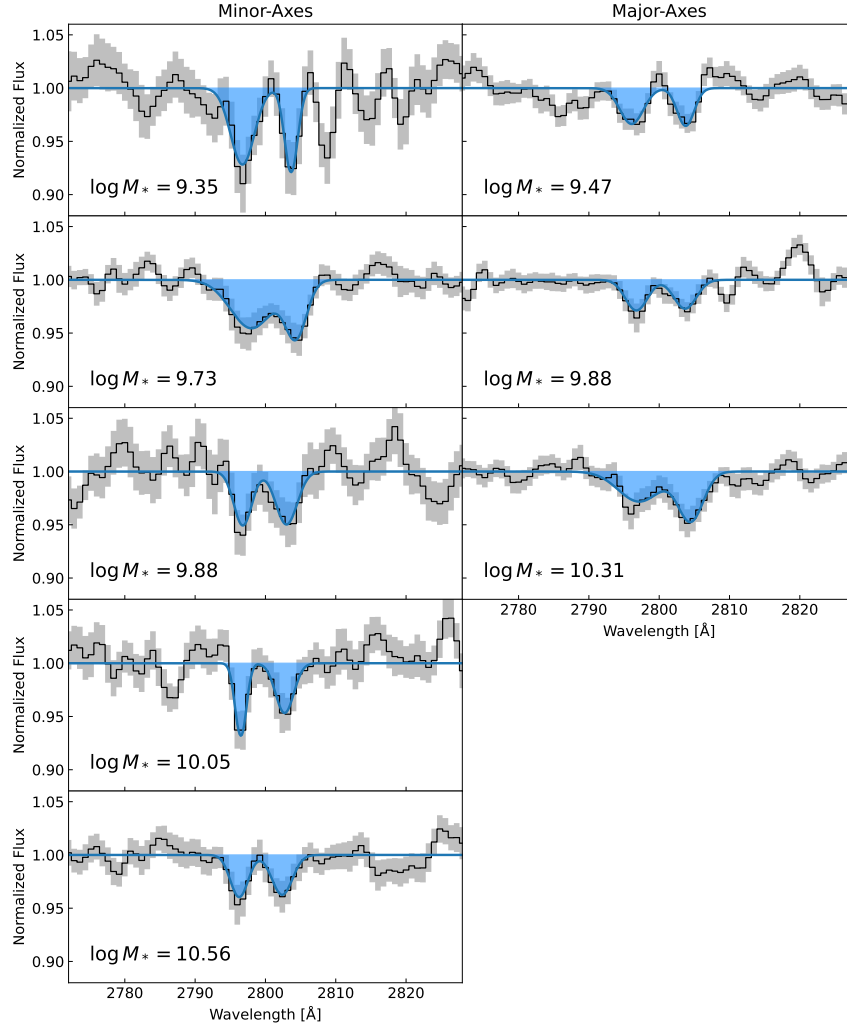


Figure S5: The stacked spectra of 20-150 kpc CGM around galaxies. The left column marked “Minor-Axes” indicates the CGM is within 45° of the minor-axes measured from the galactic center. The right column marked “Major-Axes” indicates the CGM is within 45° of the major-axes. The black line represents the median spectra and the grey shaded area indicates error derived from bootstrapping. The blue line represents the fitted double Gaussian which is only for the purpose of illustration. The EW of the absorption is calculated through integrating across the wavelengths within 3σ of the fitted Gaussian model.

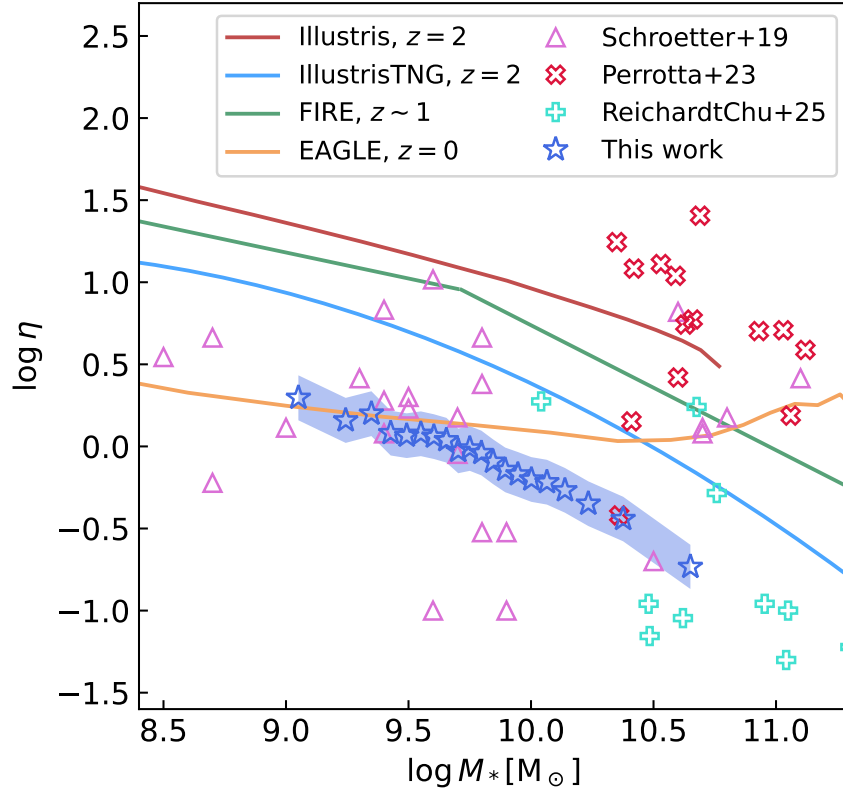


Figure S6: The derived mass-loading factor in comparison with simulations and other observations. The blue open stars and shaded area represent η and the 1σ uncertainties derived in this work. The lines are taken from papers of corresponding simulations, the M_* values of which are converted from M_{halo} through M_* - M_{halo} relation. The other open symbols represent results from observations.

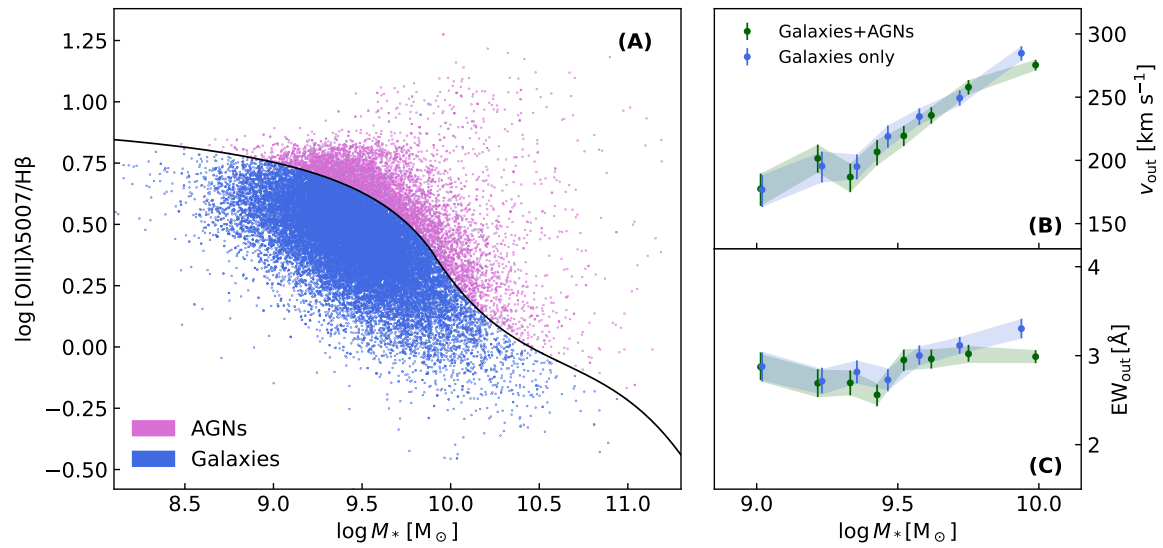


Figure S7: Evaluation of AGN contamination. (A) the flux ratio $[\text{OIII}]/\text{H}\beta$ as a function of stellar mass, where the black curve separates AGNs (represented by pink symbols) from normal star forming galaxies (represented by blue symbols). (B) v_{out} as a function of stellar mass. The green symbols represents the results before removing AGNs while the blue symbols represents the results after discarding AGNs from the sample. (C) EW_{out} as a function of stellar mass.